Mapping developmental maturation of inner hair cell ribbon synapses in the apical mouse cochlea

Susann Michanski[a,b], Katharina Smaluch[b,c,d,1], Anna Maria Steyer[e,f,1], Rituparna Chakrabarti[a,b], Cristian Setz[b,c,d,g,h], David Oestreicher[c,d,g], Christian Fischer[i], Wiebke Möbius[e,f], Tobias Moser[b,c,f,h,j], Christian Vogl[b,c,d,h,2], and Carolin Wichmann[a,b,h,2]

[a]Molecular Architecture of Synapses Group, Institute for Auditory Neuroscience, InnerEarLab and Center for Biostructural Imaging of Neurodegeneration, University Medical Center Göttingen, 37075 Göttingen, Germany; [b]Collaborative Research Center 889, University of Göttingen, 37075 Göttingen, Germany; [c]Institute for Auditory Neuroscience and InnerEarLab, University Medical Center Göttingen, 37075 Göttingen, Germany; [d]Presynaptogenesis and Intracellular Transport in Hair Cells Junior Research Group, Institute for Auditory Neuroscience and InnerEarLab, University Medical Center Göttingen, 37075 Göttingen, Germany; [e]Electron Microscopy Core Unit, Department of Neurogenetics, Max Planck Institute of Experimental Medicine, 37075 Göttingen, Germany; [f]Center Nanoscale Microscopy and Molecular Physiology of the Brain, University of Göttingen, 37075 Göttingen, Germany; [g]Department of Otolaryngology, Head and Neck Surgery, University Medical Center Göttingen, 37075 Göttingen, Germany; [h]Auditory Neuroscience Group, Max Planck Institute of Experimental Medicine, 37075 Göttingen, Germany; [i]Johann Friedrich Blumenbach Institute for Zoology and Anthropology, Department of Animal Evolution and Biodiversity, Georg August University of Göttingen, 37073 Göttingen, Germany; and [j]Synaptic Nanophysiology Group, Max Planck Institute for Biophysical Chemistry, 37077 Göttingen, Germany

Edited by Paul A. Fuchs, The Johns Hopkins University School of Medicine, Baltimore, MD, and accepted by Editorial Board Member Jeremy Nathans February 14, 2019 (received for review July 18, 2018)

Ribbon synapses of cochlear inner hair cells (IHCs) undergo molecular assembly and extensive functional and structural maturation before hearing onset. Here, we characterized the nanostructure of IHC synapses from late prenatal mouse embryo stages (embryonic days 14–18) into adulthood [postnatal day (P)48] using electron microscopy and tomography as well as optical nanoscopy of apical turn organs of Corti. We find that synaptic ribbon precursors arrive at presynaptic active zones (AZs) after afferent contacts have been established. These ribbon precursors contain the proteins RIBEYE and piccolino, tether synaptic vesicles and their delivery likely involves active, microtubule-based transport pathways. Synaptic contacts undergo a maturational transformation from multiple small to one single, large AZ. This maturation is characterized by the fusion of ribbon precursors with membrane-anchored ribbons that also appear to fuse with each other. Such fusion events are most frequently encountered around P12 and hence, coincide with hearing onset in mice. Thus, these events likely underlie the morphological and functional maturation of the AZ. Moreover, the postsynaptic densities appear to undergo a similar refinement alongside presynaptic maturation. Blockwise addition of ribbon material by fusion as found during AZ maturation might represent a general mechanism for modulating ribbon size.

synaptogenesis | presynaptic development | ribbon synapse maturation | synaptic heterogeneity

In mammals, synaptic sound encoding occurs at the first auditory synapse between cochlear inner hair cells (IHCs) and postsynaptic neurites of afferent spiral ganglion neurons (SGNs). The highly specialized IHC presynaptic active zones (AZs) are characterized by the presence of proteinaceous electron-dense bodies, called "synaptic ribbons," which are primarily composed of the structural cytomatrix protein RIBEYE (1, 2). Ribbons provide presynaptic scaffolding, cluster and functionally regulate presynaptic Ca^{2+} channels at the AZ membrane (3–5), and tether a halo of synaptic vesicles (SVs) (6). This latter feature is thought to enable rapid and indefatigable vesicular replenishment to the release site—even during periods of persistent stimulation (3, 5, 7, 8).

In mice, hearing onset occurs around postnatal day (P)12 (9) before which, IHC presynaptic AZs undergo a range of structural and functional refinements. For example, extrasynaptically localized Ca^{2+} channels are progressively eliminated from the nonsynaptic basolateral plasma membrane and form—in concert with the corresponding postsynaptic glutamate receptor patches—tightly confined clusters at mature presynaptic AZs (3, 10). Moreover, otoferlin—a large Ca^{2+}-binding multi-C_2 domain protein (11, 12)—likely replaces synaptotagmins as the putative Ca^{2+} sensor of IHC release during the first postnatal week (13). This finding reflects a key landmark of functional maturation of this unconventional high-throughput release machinery and is essentially required to faithfully orchestrate vesicular fusion in mature IHCs (14). Finally, this developmental period is critical for shaping the presynaptic morphology, reducing ribbon counts per synapse and hence, establishing the characteristic monosynaptic connectivity between IHCs and postsynaptic SGNs (10, 15–17).

To date, the temporal sequence and underlying molecular mechanisms of AZ assembly, ribbon formation as well as maturation remain to be clarified. In this context, two main—not mutually exclusive—scenarios could be envisioned: (*i*) individual cytoplasmic RIBEYE molecules may condense directly at the presynaptic scaffold to form rigid (but volatile) ribbons through continuous addition and diffusional exchange of RIBEYE molecules;

Significance

Hearing relies on temporally precise and indefatigable transmission of sensory information mediated by inner hair cell (IHC) ribbon synapses. Synaptic ribbons are electron-dense structures that tether numerous vesicles at the active zone (AZ) and drive neural encoding of acoustical signals by neurotransmitter release. The mechanisms of ribbon formation, AZ targeting and subsequent functional maturation in murine IHCs remain elusive. By combining various high-resolution imaging techniques, we analyzed multiple developmental stages and provide a new hypothesis for the assembly of auditory ribbon synapses from the apical cochlear turn. Our findings suggest that fusion of presynaptic ribbons contributes to the morphological AZ development that is essential for the functional maturation of afferent synaptic transmission within the cochlea.

Author contributions: C.V. and C.W. designed research; S.M., K.S., A.M.S., R.C., C.S., D.O., C.F., W.M., C.V., and C.W. performed research; S.M. and C.V. analyzed data; and S.M., T.M., C.V., and C.W. wrote the paper.

The authors declare no conflict of interest.

This article is a PNAS Direct Submission. P.A.F. is a guest editor invited by the Editorial Board.

[1]K.S. and A.M.S. contributed equally to this work.

[2]To whom correspondence may be addressed. Email: christian.vogl@med.uni-goettingen.de or carolin.wichmann@med.uni-goettingen.de.

This article contains supporting information online at www.pnas.org/lookup/suppl/doi:10.1073/pnas.1812029116/-/DCSupplemental.

Published online March 13, 2019.

or alternatively, (*ii*) preformed RIBEYE aggregates may undergo targeted transport to the basolateral plasma membrane to finally fuse to each other at (or in close proximity to) the AZ. Such ribbon precursors have previously been reported in the cytoplasm of retinal photoreceptors (18), hair cells of zebrafish lateral line neuromasts (19), the chicken basilar papilla (20), and also in mammalian auditory hair cells (17, 21). However, a detailed study of their cellular origin, molecular composition, mode of transport, and role of these precursors in AZ formation in IHCs is lacking to date. In photoreceptors, ribbon precursors were shown to contain not only RIBEYE, but also other cytomatrix proteins such as bassoon, piccolino, and RIM1 (18).

Here, we performed a comprehensive morphological analysis of IHC ribbon synapse development in mice—spanning from shortly before birth into adulthood—to advance the understanding of their formation and maturation. To do so, we combined transmission electron microscopy (TEM), electron tomography, focused ion beam-scanning electron microscopy (FIB-SEM) as well as serial block face-scanning electron microscopy (SBF-SEM) and stimulated emission-depletion (STED) optical nanoscopy. We found that IHC ribbon precursors contain piccolino and RIBEYE and reside in close proximity to IHC AZs from embryonic stage (E)18 onwards. Using temporal mapping of several synaptic parameters, we documented the developmental changes of IHC synapses in the run-up to hearing onset. With this systematic approach, we identified a transient developmental period directly before the onset of hearing, where fusion events of synaptically anchored ribbons appear to take place with increased frequency, thereby establishing the mature presynaptic morphology and increasing the vesicular tethering capacity that is essential for indefatigable release. Moreover, our data suggest that ribbon precursors employ an active mode of transport for targeted delivery to the presynaptic AZ.

Results

Afferent Contact Formation Precedes Presynaptic Ribbon Attachment at IHC AZs. To investigate the developmental assembly and maturation of IHC ribbon synapses of apical turn organs of Corti, we performed a detailed ultrastructural analysis ranging from late embryonic stages into adulthood. In these experiments, we selected narrow age groups that seamlessly covered the entire developmental period before hearing onset and beyond (i.e., E14, E16, E18, P0–1, P2–4, P9, P12, P14–15, P19–20, P34/P48). In a first experimental set, we investigated the basolateral regions of E14, E16, and E18 IHCs to determine initial AZ formation (*SI Appendix*, Fig. S1 *A–C′*). Here, differentiated IHCs could be identified as early as E14, with the first detectable afferent fiber contacts by E16—a finding consistent with previous reports (15, 22–24). Interestingly, before E18, we never observed synaptic ribbons, SVs, or obvious electron-dense AZ specializations of any kind at these early stages (*SI Appendix*, Fig. S1 *A–B′*). In contrast, from E18 onwards, small cytoplasmically floating as well as membrane-attached ribbon precursors could be detected juxtaposed to developing postsynaptic densities (PSDs) (*SI Appendix*, Fig. S1 *C–C′*). Hence, we conclude that afferent contacts are established before the arrival of ribbon precursors at IHC AZs.

Upon Maturation, Ribbon Size and SV Number Increase, While SV Diameter and Ribbon Number per AZ Are Progressively Reduced. Next, we performed a comparative analysis of IHCs of all age groups that possess synaptic ribbons (E18–P48). In these experiments, we initially concentrated on general morphological features of IHC presynaptic AZs, such as ribbon size and number (Fig. 1 *A–F*), as well as additional parameters, including SV diameter and counts in random ultrathin 2D sections of conventionally embedded organs of Corti (Fig. 1 *G* and *H*). In embryonic and early postnatal IHCs, we mostly found accumulations of

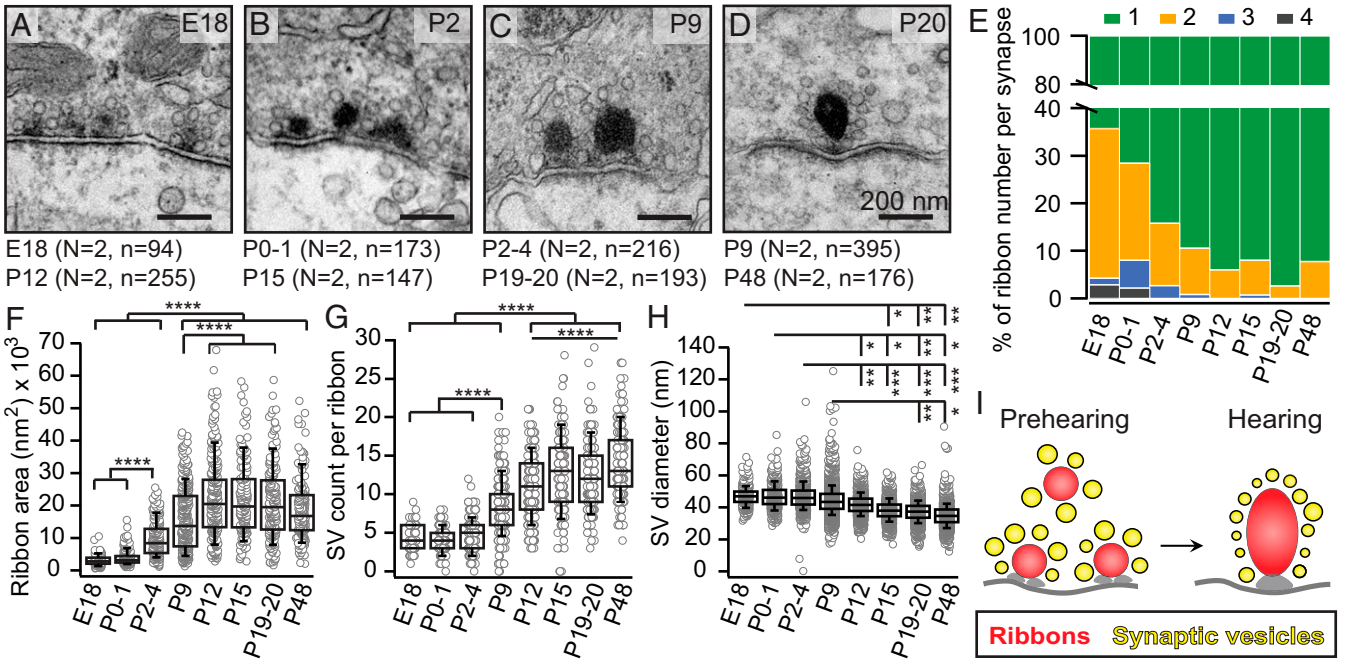

Fig. 1. Synaptic ribbon size and SV number steadily increases until hearing onset; SV maturation is accompanied by a decrease in SV size. (*A–D*) Representative electron micrographs of the indicated age groups, illustrating IHC presynaptic contacts either decorated with multiple or single synaptic ribbons. (*E*) Frequency of occurrence of the indicated ribbon number per afferent contact and age group. Random section analysis of (*F*) ribbon area, (*G*) SV count per ribbon, and (*H*) SV diameter. *N* = animal number, *n* = ribbon number. Data are represented as box plots showing 10, 25, 50, 75, and 90th percentiles with individual data points overlaid. For detailed statistical evaluation see *SI Appendix*, Table S1. **P* < 0.05, ***P* < 0.01, ****P* < 0.001, *****P* < 0.0001. (*I*) Schematic drawing summarizing the main morphological features affected by developmental maturation.

small round ribbons that exhibited multiple attachment points at the presynaptic plasma membrane. In contrast, after the onset of hearing, larger ribbons with a single continuous membrane anchor dominated the presynaptic morphology (Fig. 1 *A–E*), as shown previously (10, 17). Next, we mapped developmental changes in ribbon size by measuring maximal ribbon height, width, and area excluding the presynaptic density (Fig. 1*F* and *SI Appendix*, Fig. S2 *A–C*). Our data indicate that synaptic ribbons continuously grow before reaching their mature size at hearing onset at ~P12 (Fig. 1*F* and *SI Appendix*, Table S1). Interestingly, we observed fenestrated "hollow" ribbons that occurred from P9 onwards (0.40%), as previously described for ribbons of different ages (17, 25). Their proportion increased to ~17% during maturation, but remained remarkably stable after hearing onset (*SI Appendix*, Fig. S2 *D–F*).

For the characterization of presynaptic SV populations, we counted the number of SVs in the first layer around the ribbon within a maximum distance of 80 nm (*SI Appendix*, Fig. S2 *A* and *A′*) and observed a steady increase in SV number per ribbon upon maturation (Fig. 1*G* and *SI Appendix*, Fig. S2*G* and Table S1; from E18: 4.48 ± 0.16 to P48: 13.98 ± 0.36; $P < 0.0001$ nonparametric multiple comparison test). Intriguingly, the mean SV diameter continuously decreased in the run-up to hearing onset, but stabilized thereafter (Fig. 1*H* and *SI Appendix*, Fig. S2*H* and Table S1; from E18: 47.00 ± 0.28 nm to P48: 34.86 ± 0.13 nm; $P = 0.0052$ Kruskal–Wallis test).

In summary, our data show that AZs of immature IHCs are mainly occupied by multiple small ribbons that are surrounded by large SVs. In contrast, AZs of mature IHCs displayed large, predominantly single ribbons that harbor a larger population of smaller-sized SVs (Fig. 1*I*).

Postsynaptic Maturation Is Characterized by a Transition from Several Small PSDs to One Single, Continuous PSD. Previously, we could show that PSD length increases upon maturation from P6 to P20 (10). To now gain more detailed and time-resolved insights into this process, we quantitatively analyzed the number of PSDs per afferent contact and measured individual PSD length in random ultrathin sections of all aforementioned age groups (*SI Appendix*, Fig. S3 *A* and *B*). In these experiments and in contrast to previous findings (21), we could clearly identify individual PSDs from E18 onwards and observed a progressive decrease in PSD number per AZ alongside an increase in PSD length throughout pre- and postnatal maturation (*SI Appendix*, Fig. S3 *C* and *D* and Table S2). From these observations we propose that, upon maturation, several small PSDs merge into a single large PSD (*SI Appendix*, Fig. S3*E*).

Fusion of Ribbon Precursors Is a Critical Step in Presynaptic AZ Maturation and Determines the SV Tethering Capacity. Consistent with previous reports (21), we frequently observed "floating ribbons" in close proximity to membrane-anchored ribbons, primarily in IHCs of prehearing animals, which likely represent ribbon precursors (Fig. 2 *A* and *E* and *SI Appendix*, Fig. S4 *A* and *B*). These floating ribbons were decorated with a full set of SVs and could also be observed in mature animals, though at drastically reduced frequency. Interestingly, we observed putative fusion events of floating and membrane-anchored ribbons (Fig. 2 *B* and *C* and *SI Appendix*, Fig. S4 *C* and *D*) that have also recently been described to occur in zebrafish lateral line neuromast hair cells (19). In mouse IHCs, these events encompassed apparent fusion of (*i*) two membrane-attached ribbons at the same presynaptic AZ (Fig. 2*B*), (*ii*) clusters of floating ribbon precursors (Fig. 2*C*), and (*iii*) small floating ribbon precursors with membrane-attached ribbons (*SI Appendix*, Fig. S4 *C* and *D*).

From P12, we found a clear drop in the number of floating ribbons (Fig. 2*E*) and overall ribbon counts per synapse, suggesting a dedicated cellular mechanism that streamlines AZ morphology. Two main scenarios can be envisioned in this context: either (*i*) fusion of ribbon precursors to form single AZ ribbons or (*ii*) pruning of surplus ribbons via degradation. To now differentiate between these scenarios, we analyzed random single EM sections alongside two-color 2D STED images. Here, while we predominantly observed these events around the onset of hearing (P12) in our EM analysis of random ultrathin sections (Fig. 2*E*), the increased sample screening capacity of immunohistochemistry and STED microscopy allowed us to identify these events in a wider developmental time window. Indeed, our analysis confirmed the existence of ribbon shapes indicative of fusion at AZs also in P7 and P14 IHCs (Fig. 2*F*), thereby suggesting a broader time interval of ribbon fusion occurrence that

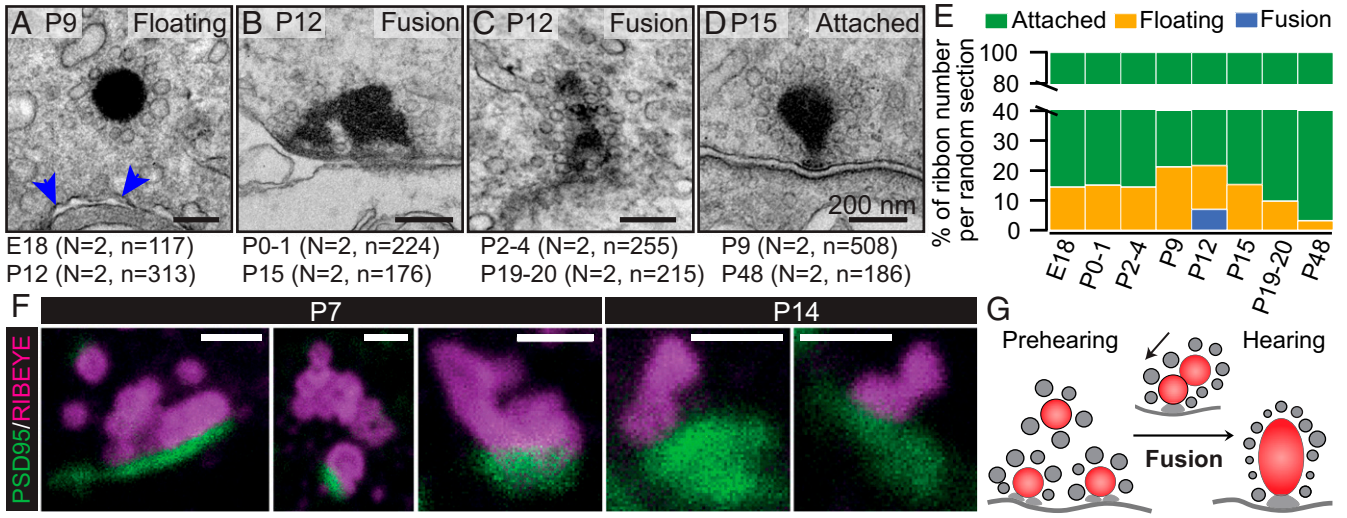

Fig. 2. Ribbon precursor fusion is critical for AZ maturation. Representative electron micrographs showing (*A*) a cytoplasmically floating ribbon precursor in close vicinity to the IHC membrane (blue arrowheads), (*B* and *C*) apparent ribbon fusion events, and (*D*) a fully mature and membrane-attached ribbon. (*E*) While the proportion of membrane-attached ribbons increased upon maturation (from 85.47% in E18 to 96.77% in P48), the number of floating ribbons declines (from 14.53% in E18 to 3.23% in P48). *N* = animal number, *n* = ribbon number. (*F*) STED optical nanoscopy revealed putative ribbon fusion events before and after the onset of hearing (P7 and P14, respectively). (Scale bars: 500 nm.) (*G*) Schematic illustrating ribbon synapse maturation via ribbon precursor fusion.

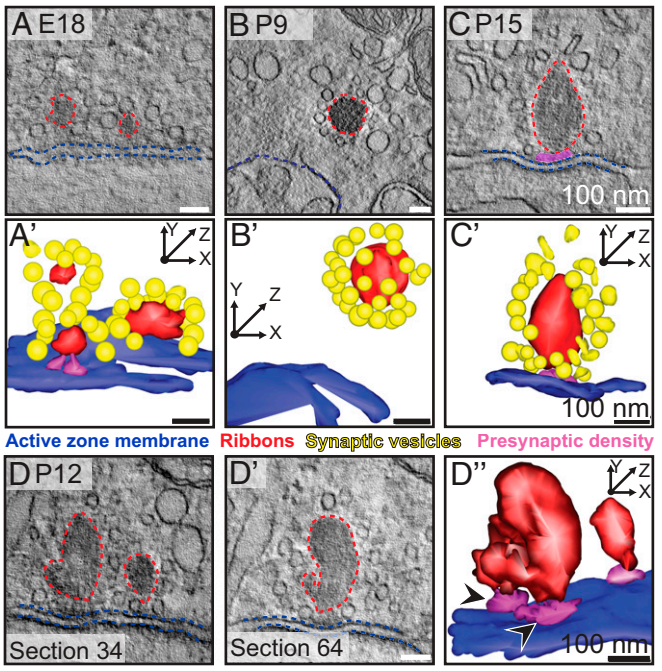

Fig. 3. Floating ribbon precursors and ribbon fusion processes observed at synaptically anchored ribbons around the onset of hearing. (*A*–*C*) Single tomographic virtual sections of ribbons before (E18, P9) and after (P15) the onset of hearing. Ribbons, red dashed line; AZ membrane, blue dashed line; presynaptic density, magenta in *C*. (*A*′–*C*′) Tomogram 3D models depicting several floating ribbons in immature IHCs (*A*′ and *B*′) as well as synaptic ribbons that are attached to the AZ membrane by a presynaptic density (*A*′ and *C*′). (*D* and *D*′) Single tomogram virtual sections and the corresponding 3D reconstructions of fusing ribbons in P12 IHCs (*D*″). For better visualization of the contacts between the ribbons, SVs were removed from the 3D model. Please note that both fusing ribbons in *D*″ are attached by individual single presynaptic densities (arrowheads).

even extends after hearing onset (summary in Fig. 2*G*). However, due to the nature of 2D data, false positives for floating ribbons could result from their orientation to the projection plane. Hence, to eliminate such bias, we turned to high-resolution 3D electron tomography in a small subset of samples (Fig. 3 and *SI Appendix*, Fig. S4 *E*–*F*‴). This approach confirmed the occurrence of numerous floating ribbons in immature IHCs (Fig. 3 *A*–*B*′), whereas all observed ribbons in IHCs of mature animals were attached (Fig. 3 *C* and *C*′). In addition, we found 3D indications for the occurrence of ribbon fusion events, such as (*i*) a smaller ribbon connected to a large AZ-anchored ribbon, (*ii*) an additional small AZ-attached ribbon, or (*iii*) floating precursor ribbons next to fusing ribbons (Fig. 3 *D*–*D*″ and *SI Appendix*, Fig. S4 *E*–*F*‴).

To now investigate ribbon synapse maturation over a wider developmental range (i.e., P7–P14, with a focus on P10–12), we employed two-color 2D STED optical nanoscopy (Fig. 4). In these experiments, we selected the maximum intensity planes of large amorphously shaped RIBEYE-immunoreactive spots that were juxtaposed to a clearly demarcated PSD95 cluster (as initially assessed at confocal resolution) for STED imaging (Fig. 4 *A* and *B*). We focused our analysis on optical planes, where we could clearly establish synaptic orientation (i.e., based on PSD95 cluster shapes: either side profiles or direct en face "top" views; Fig. 4 *B* and *C*). Here, the high lateral resolution of 2D STED nanoscopy facilitated the distinction of individual ribbons at a given synapse and revealed a large number of multiribbon synapses in samples from >P7 IHCs. These ribbons progressively increased in size and decreased in number toward hearing onset, consistent with the fusion of initially separate—though membrane-anchored—ribbon complexes. Finally, synapses from ~P12 onwards appeared to harbor large, predominantly single ribbons (Fig. 4*C*). Therefore, although we cannot fully exclude the possibility of an additional pruning mechanism degrading surplus membrane-anchored ribbons, our data clearly favor the fusion hypothesis. To further test this, we aimed to quantify the RIBEYE-occupied volume per AZ across all age groups. However, due to the high STED laser powers required to obtain sufficient lateral resolution and the concomitant photobleaching resulting from 3D data acquisition as well as the varying size and distribution of ribbon precursors at individual AZs (e.g., ring-shaped ribbon clusters or double row configurations of 2 × 3 ribbons in Fig. 4*C*), we refrained from quantitative analysis of these data. Future live-cell experiments will be required to ultimately clarify this issue, but recent evidence from zebrafish lateral line neuromast hair cells (19) further supports the fusion hypothesis.

Dense-Core Vesicles Appear in Close Proximity to IHC Presynaptic AZs During Early Development (E18–P4). Interestingly, in addition to ribbon precursors, we detected dense-core vesicles (DCVs) close to IHC AZs in E18–P4 animals (*SI Appendix*, Fig. S4 *G*–*J*) in our ultrastructural analysis. DCVs exhibit a characteristic spherical

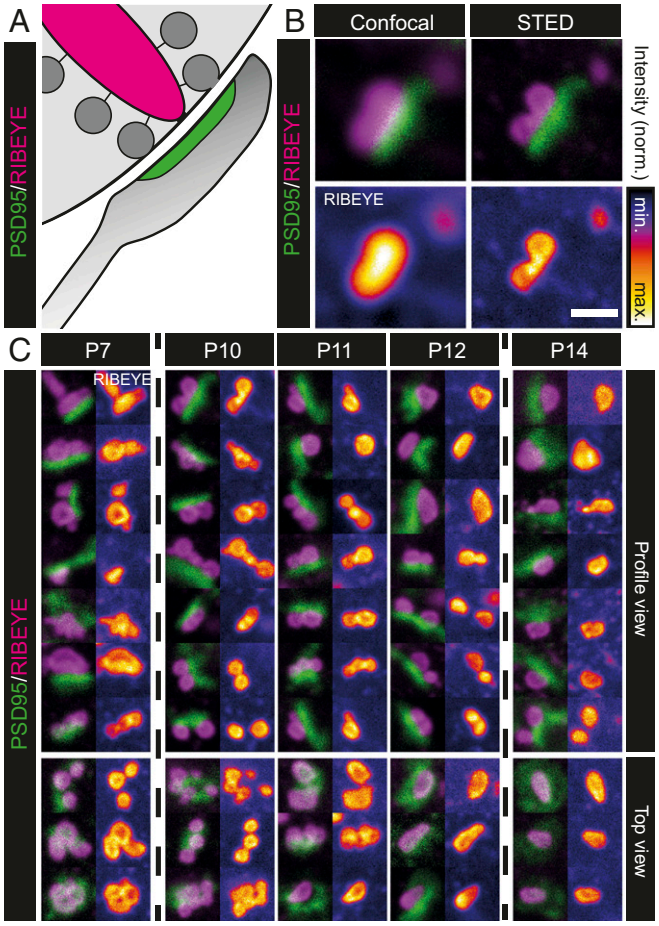

Fig. 4. Nanoscopic analysis of the morphological maturation of cochlear IHC ribbon synapses. (*A*) Schematic illustration of the mature experimental site and the labeled pre- and postsynaptic structures. (*B*) Profile views of an individual synapse (P10) in confocal and STED mode to illustrate the merits of improved lateral resolution. (*C*) Representative IHC synapse profiles highlighting the developmental transition from multiribbon complexes to predominantly single ribbon synapses. In the *Insets* in *B* and *C*, individual RIBEYE channels are presented separately with an intensity-coded look-up table for clarity (warmer colors indicate higher intensity). (Scale bar in *B*: 500 nm; in *C*: each box is 1 × 1 μm.)

shape with electron-dense core and are easily distinguishable from SVs; however, the very low overall density, small but highly variable size (~50 nm < DCV < ~180 nm, *SI Appendix*, Fig. S4*J* and Table S2) and apparently temporally tightly confined occurrence of these structures limited their analysis in our preparation. At conventional synapses, DCVs have been proposed to be involved in AZ assembly by two different mechanisms: (*i*) a subpopulation of DCVs has been shown to contain neurotrophins, that may be required for axonal pathfinding and synapse formation (26–31); and (*ii*) DCVs have been implicated in the targeted transport of several AZ proteins to the presynaptic membrane (e.g., piccolo and bassoon) (32–34). Unfortunately, our efforts to clarify the nature of these DCVs in cochlear IHCs by immuno-EM, so far, have not been successful. For example, we tested for the expression of piccolino (the C-terminal truncated isoform of piccolo expressed in IHCs; ref. 36) on DCVs and performed preembedding immunogold labelings against piccolo using an antibody that recognizes both the short and the long piccolo isoforms (35), but were not able to detect labeled DCVs. Moreover, both preembedding immunogold labeling against bassoon in IHCs of prehearing animals as well as the immunohistochemical stainings for brain-derived neurotrophic factor (Bdnf) remained unspecific, rendering the molecular nature of DCVs elusive.

Putative Involvement of Microtubules in Ribbon Precursor Transport. Interestingly, in our electron micrographs and EM tomograms, we regularly observed cytoplasmic ribbon precursors that were lined up alongside microtubules (MTs) in various instances (~25%), a finding that may suggest active cytoskeletal transport (Fig. 5 *A* and *B* and *SI Appendix*, Fig. S5 *A–B′*). Subsequent STED analysis confirmed the close approximation of CtBP2-positive synaptic ribbons and α-tubulin containing MTs within the IHC basolateral compartment (Fig. 5*C*). To address this in more detail, we measured the distance of the closest precursor-associated SV (PA-SV) to adjacent MTs in electron micrographs of P9 IHCs (Fig. 5*D*) and found a highly skewed distance distribution with a clear accumulation of PA-SVs in close proximity to MTs (median shortest distance: 32.92 nm; Fig. 5*D′*). The observed distance is compatible with kinesin-based MT/cargo interaction (25–30 nm for kinesin isolated from bovine brain; ref. 37) supporting our hypothesis of molecular motors linking MTs and PA-SVs. Together, these findings may suggest the involvement of an as-yet-undescribed MT-based transport system that actively shuttles ribbon precursors to the AZ. In an attempt to identify putatively involved molecular motors linking PA-SVs to MTs, we next performed immunohistochemical screening for selected kinesins and analyzed their association with RIBEYE- or CtBP2-positive structures in IHCs. Guided by previously published RNA-sequencing data of developing IHCs (38), we concentrated our efforts on motors with the highest overall IHC expression levels that were additionally reported to be involved in organelle or SV/DCV precursor transport, such as the MT plus end directed motors KIF1a, KIF2a, and KIF5 (Fig. 5*E* and *SI Appendix*, Fig. S5 *C–E′*) (39). Here, our data are consistent with a potential involvement of KIF1a (Fig. 5*E* and *SI Appendix*, Fig. S5 *C* and *C′*)—but not KIF2a or KIF5a–c (*SI Appendix*, Fig. S5 *D–E′*)—in ribbon precursor transport, as spot-like association of KIF1a with ribbon precursors could be observed on various occasions and may suggest motor/cargo interaction (*SI Appendix*, Fig. S5*C′*). However, future live-cell analysis will be required to fully clarify this issue.

Insights into the Molecular Constituents of Developing Ribbons. In line with previous work on retinal preparations (18, 36), we detected piccolino on floating ribbon precursors as well as membrane-attached ribbons from P2 throughout the course of development (probed at P2, P9, P14, and P21) using both, preembedding immunogold EM labeling and immunohistochemistry followed by STED microscopy (Fig. 6 *A–D′* and *SI Appendix*, Fig. S6 *A–D*). Consistent with previous immunogold EM studies of photoreceptor ribbons (35, 40), CtBP2-labeling identified RIBEYE as the main component of the ribbon (1) and was detected across the whole surface of the ribbon, independent of the developmental age (*SI Appendix*, Fig. S6 *E–L*). Interestingly, until ~P14, piccolino was seen to be predominantly localized at the upper part of the ribbons by both STED microscopy (Fig. 6 *A–C*) and immunogold EM (Fig. 6 *A′–C′* and *SI Appendix*, Fig. S6 *A* and *C*), but also extended toward the ribbon base thereafter

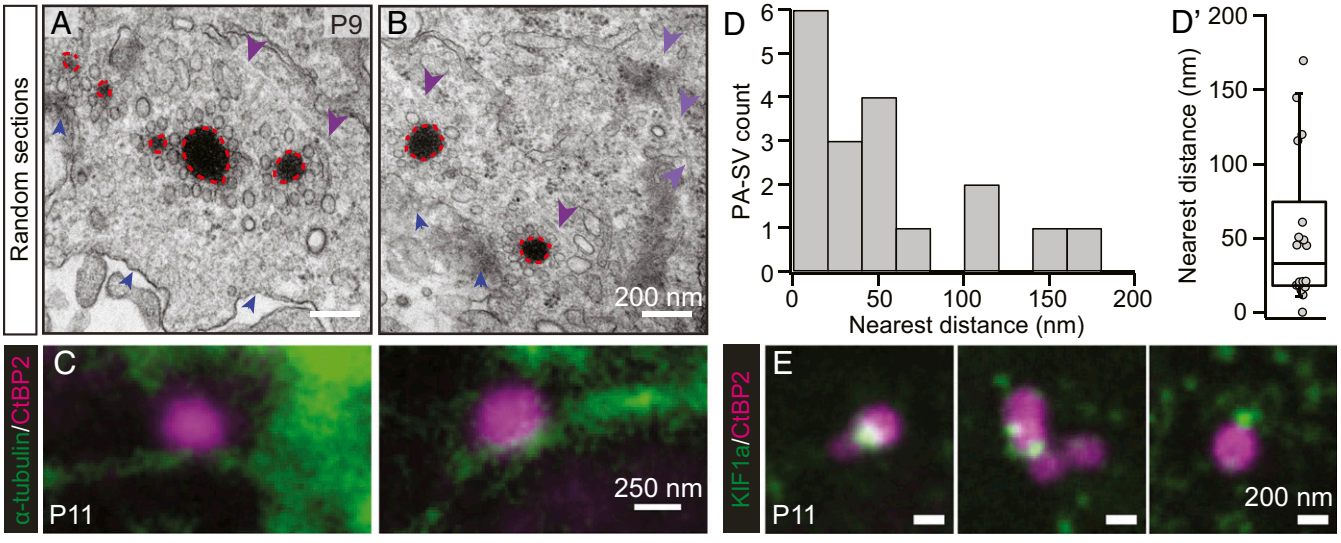

Fig. 5. Potential transport of ribbon precursors along MTs. (*A* and *B*) Exemplary electron micrographs of multiple ribbon precursors (dashed red line), in close proximity to MTs (larger purple arrowheads) and the IHC membrane (smaller blue arrowheads) in prehearing mice. (*C*) Single STED optical sections of IHCs immunostained for α-tubulin (green) and CtBP2 (magenta) showing close association of ribbons and MTs. (*D* and *D′*) Quantification of the nearest distance of PA-SVs within 200 nm perimeter around longitudinally cut MTs. (*E*) STED imaging of KIF1a-labeled (green) IHCs counterstained with the ribbon marker CtBP2 (magenta) revealed close association of the two target proteins.

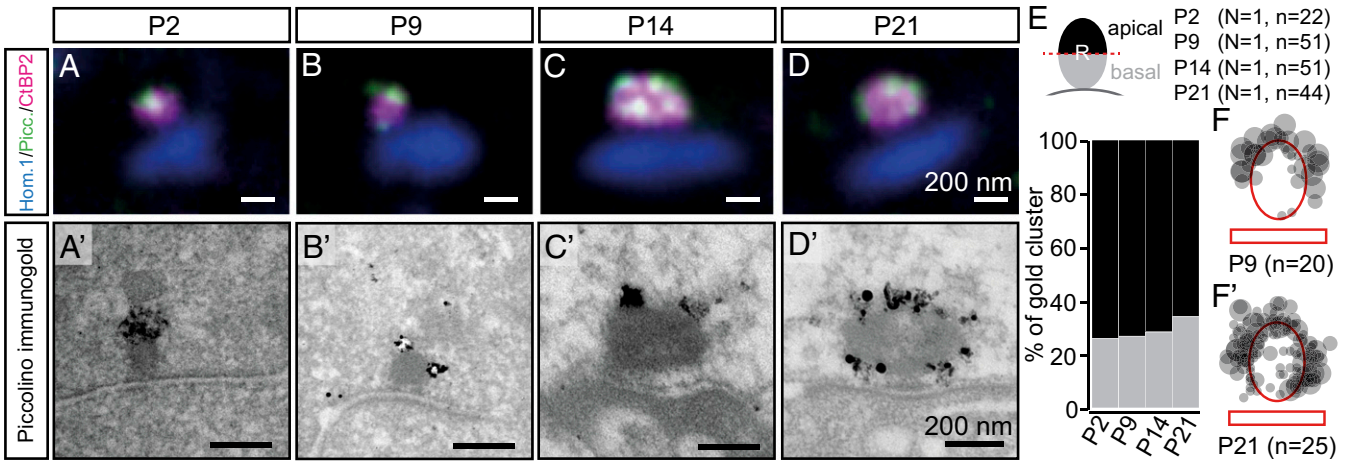

Fig. 6. Distribution of piccolino at maturing ribbons. At P2 (*A* and *A′*), P9 (*B* and *B′*), and P14 (*C* and *C′*), piccolino immunoreactivity concentrates at the apical part of the ribbon, but progressively redistributes toward the lower ribbon half by P21 (*D* and *D′*) as observed in STED (*A–D*) and with immunogold EM (*A′–D′*). (*E*) Bar graph representing the percentage of gold cluster occurrence in preembedding immunogold labelings at the apical and basal ribbon (R) half upon maturation (*N* = animal number, *n* = ribbon number). (*F* and *F′*) Schematic illustrations of the position of differently sized antipiccolino immunogold particles (gray circles) overlaid from all quantified ribbons, highlighting the distinct piccolino distribution between P9 and P21 IHCs. Red oval-shaped circles outline the ribbon; red boxes *Below* indicate the IHC plasma membrane.

(Fig. 6 *D* and *D′* and *SI Appendix*, Fig. S6*D*), thus indicating maturational redistribution of piccolino localization (Fig. 6 *E–F′*).

In summary, we demonstrate substantial morphological changes of afferent IHC synapses from prehearing to hearing regarding (*i*) SV diameter as well as number, (*ii*) ribbon size and counts per afferent contact, and finally (*iii*) number of ribbon precursors floating in the cytoplasm. In addition, we observed that synaptic ribbons appear to fuse at increased frequency around the onset of hearing. Finally, we found evidence for a kinesin-based ribbon precursor transport pathway operating in IHCs.

Next, we asked whether the number of ribbons as well as their size distributes in a predetermined spatial pattern within an individual IHC and if so, whether such a distribution is already established before hearing onset.

Establishing IHC Ribbon Synapse Heterogeneity. Consistent with previous work (10, 17, 41), our analyses of ultrathin sections, EM tomograms, and immunohistochemistry revealed a high degree of diversity regarding ribbon shapes and sizes, even in functionally mature IHCs. In addition to the already described developmental decline in ribbon number, confocal imaging further revealed a high variability in ribbon morphology within individual IHCs ("presynaptic heterogeneity," Fig. 7*A* and *A'*). This heterogeneity has previously been described for cats and mice, where ribbon size as well as number and voltage-dependent activation of Ca^{2+} channels strongly depend on the subcellular localization (16, 41–44). Accordingly, synapses localized at the modiolar (neural) side of the IHCs appear to contain large or multiple ribbons per AZ and drive low spontaneous rate, high threshold SGNs, whereas smaller ribbons commonly oppose high spontaneous rate, low threshold neurons, and are mostly situated at the pillar (abneural) side (16, 43, 44). To characterize the underlying subcellular processes from a developmental perspective, we utilized SBF-SEM and FIB-SEM to assess the morphological heterogeneity of ribbons from intact mouse IHCs with unprecedented spatial resolution. Both techniques allow the direct whole-cell analysis of ribbon size distribution within the context of the unperturbed tissue at a resolution level permitting quantification of individual SVs on floating and/or membrane-attached synaptic ribbons. Here, while our initial and basic quantitative analysis was performed using SBF-SEM (*SI Appendix*, Fig. S7 *I* and *J*), we finally resorted to FIB-SEM due to the greatly improved *z* resolution of this approach and, hence, more detailed quantification possibilities. In these experiments, we visualized the entire basolateral compartment, including presynaptic ribbons and postsynaptic SGN fibers (Movie S1) of two IHCs each from three selected age groups (P9, prehearing; P15, after hearing onset; and P34, mature) and determined several parameters such as ribbon number and size in regards to their subcellular position (Fig. 7 *B–E*). Here, IHCs were hemisectioned layer by layer and separated into modiolar and pillar halves (refer to *SI Appendix*, *Materials and Methods* for further details). Consistent with previous studies (25, 44, 45), we found fewer ribbons at the pillar side and a higher number of ribbons on the modiolar side across all three age groups (Fig. 7 *C–E* and *K* and *SI Appendix*, Fig. S7 *A–C*). Moreover, the ribbon shape changed from predominantly round (Fig. 7 *F* and *G*) to mature wedge- or droplet-like ribbons (Fig. 7 *H–J*), which regularly exhibited an electron-lucent core in P15 and P34 animals (Fig. 7 *H* and *J*), as described in our random sections. In line with our random section analysis, throughout IHC development, SV numbers increased with growing ribbon size, independent of the subcellular location (Fig. 7*L* and *SI Appendix*, Fig. S7*D* and Table S3). Further, multiple ribbons per afferent contact (Fig. 7 *F* and *I*) could be observed most frequently in P9 IHCs (*SI Appendix*, Fig. S7*E*). However, double and triple ribbons still occur in ∼25% of the synapses at P34, where the distances between these mature ribbons were on average shorter than those observed at multiribbon contact sites of P9 IHCs (*SI Appendix*, Fig. S7*F*). However, the shortest distances between ribbons of the nearest neighboring synapses, did not change during development (*SI Appendix*, Fig. S7*G*). Additionally, floating ribbons with an average distance of 117.22 ± 32.51 nm to the plasma membrane could be observed particularly in P9 (Fig. 7 *G* and *K* and *SI Appendix*, Fig. S7*H*) and—in contrast to previous studies (21)—solely in the basolateral, but not the supranuclear compartment (*SI Appendix*, Fig. S7*K* and Movie S2). Surprisingly, afferent fibers of all age groups exhibited ribbonless afferent contacts with IHCs (i.e., lacking synaptic ribbons, but exhibiting a clear physical contact; at 18.48% of IHC AZs)—a feature that could be observed with comparable frequency at both pillar and modiolar sides (P9, modiolar 5.7% vs. pillar 5.7%; P15, modiolar 8.0% vs. pillar 12.0%; and P34, modiolar 12.5% vs. pillar 12.5%). If these latter

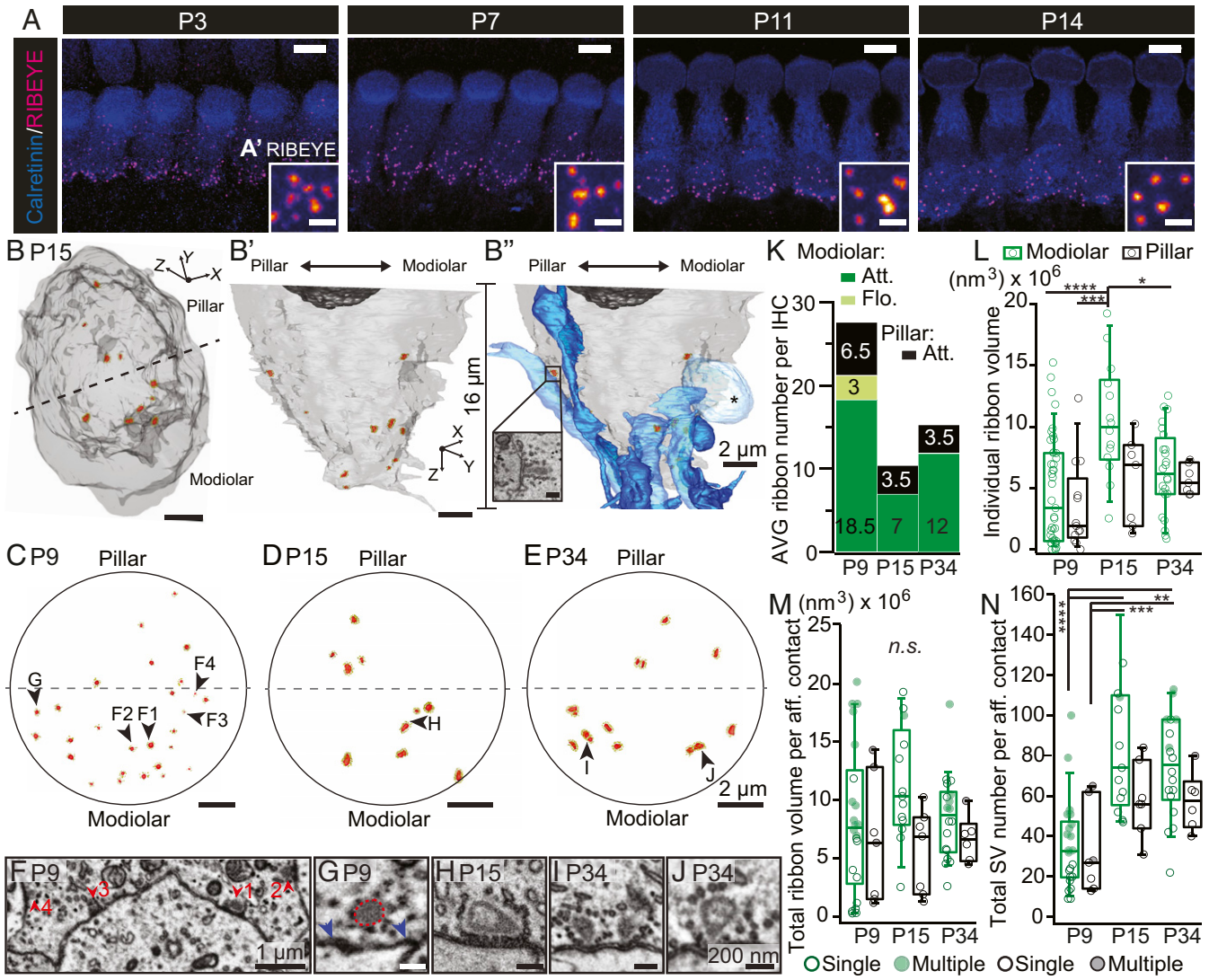

Fig. 7. Position-dependent morphological characterization of apical coil IHC AZs. (*A*) Representative confocal *z* projections of RIBEYE-labeled ribbons before and after hearing onset. (*A′*) *Insets* show close-ups of several adjacent IHC AZs for clarity. (Scale bars: 5 µm; *Insets*, 1 µm.) (*B*–*B″*) Three-dimensional visualization of the basal part of a P15 IHC using FIB-SEM displayed either in *Top* view (*B*) or *Side* view, with (*B″*) or without (*B′*) the afferent innervation. Small *Inset* shows a representative section of a reconstructed ribbon. (Scale bar: 100 nm.) Gray, IHC membrane; black, nucleus; red, ribbons; yellow, SVs; blue, afferent fibers; asterisk, swollen afferent bouton. (*C*–*E*) FIB-SEM 3D projections of ribbons (red) and SVs (yellow) throughout the basal part of IHCs at different ages viewed from the *Top*. Black arrowheads highlight ribbons that are shown in *F*–*J* by representative sections. (*F*) Red arrowheads point toward membrane-attached synaptic ribbons; blue arrowheads in *G* indicate the IHC plasma membrane with a floating ribbon precursor (red dashed line). (*H*–*J*) Exemplary ribbons after hearing onset frequently exhibited a hollow core. (*I*) Multiribbon synapses (modiolar) were still present in adult IHCs. (*K*) Absolute ribbon counts of all three age groups. Floating (Flo.) ribbons were solely present at the modiolar side (green) of maturing IHCs, but never at P34 IHCs, where all ribbons were attached (Att.). Ribbon counts at the pillar side are shown in black. $n = 2$ IHCs for each age group. (*L*) Box plots display individual ribbon size measurement data points. (*M*) Quantification of the combined ribbon-occupied volume per afferent (aff.) contact. Empty circles represent single ribbon synapses; filled circles represent the summed volume of multiribbon synapses. (*N*) Box plots showing the number of SVs per afferent contact. Higher SV counts were detected in P34 IHCs. Box plots present 10, 25, 50, 75, and 90th percentiles with individual data points overlaid (*n.s.* > 0.05, *P < 0.05, **P < 0.01, ***P < 0.001, ****P < 0.0001).

connections are indeed synaptically engaged and which, if any, role they play in cochlear sound encoding remains to be determined.

Quantification of ribbon size showed a strong trend toward increased volumes in P15 and P34 IHCs (Fig. 7*L* and *SI Appendix*, Table S3). Interestingly, analysis of the total ribbon-occupied volume per afferent contact, i.e., where all ribbons of one individual afferent contact were summed up, showed comparable mean volumes per contact between P9, P15, and P34 IHCs (Fig. 7*M* and *SI Appendix*, Table S3), thereby supporting our hypothesis that ribbon fusion, not pruning, is an essential process for structural confinement of IHC AZs. Moreover, multiple ribbons per afferent contact were predominantly found at the modiolar side of all investigated age groups (*SI Appendix*, Fig. S7*E*), thereby indicating a location dependence of afferent contact sites.

In line with our above observations, despite an overall reduction of ribbon number per AZ, SV counts per contact increased upon maturation, but remained constant after hearing onset (Fig. 7*N* and *SI Appendix*, Table S3).

Discussion

In the present study, we provide a detailed and comprehensive characterization of auditory ribbon synapse formation and maturation of murine apical coil IHCs. Using a combinatorial approach of ultrastructural analyses and superresolution microscopy, we dissected

the morphological changes of IHC presynaptic AZs with unprecedented spatial and temporal resolution, ranging from late embryonic to adult stages (summarized in Fig. 8). Specifically, we show that (*i*) afferent contacts between IHCs and SGNs are established before ribbon attachment at the presynaptic membrane; (*ii*) ribbon size and SV numbers per AZ increase rapidly until hearing onset, while SV diameter successively decreases during maturation; (*iii*) ribbon precursors as well as membrane-anchored ribbons seem to fuse at the presynaptic membrane to generate mature, predominantly single ribbons; (*iv*) cytoplasmic ribbon precursors appear to employ an active, MT-based mode of transport to the AZ; (*v*) independent of their developmental age or subcellular location, piccolino seems to be an integral part of IHC ribbons; and finally, (*vi*) presynaptic morphological heterogeneity is established before hearing onset and a fraction of—predominantly modiolar—multiribbon AZs persist into adulthood. Therefore, this study provides deeper insights into the developmental assembly and molecular maturation of these remarkable synapses.

Establishment of Synaptic Connectivity at IHCs. Afferent fibers approaching IHCs could be observed as early as E16; however, in accordance with previous findings (15, 22–24), first ribbon attachment and initiation of synapse formation occurs at ∼E18. Our data indicate that synaptic contact formation—as characterized by a clearly demarcated pre- and postsynaptic density—often precedes ribbon attachment at the AZ membrane. Hence, these findings contradict previous work, which suggested that presynaptic AZ assembly in IHCs initiates PSD formation in afferent neurites (21). The temporal sequence of events forming a fully mature ribbon-type AZ still needs to be defined; however, recent studies on *RIBEYE*-KO mice indicate that, in IHCs, features like PSDs, presynaptic densities, and the presence of Ca^{2+} channels and bassoon develop independently of ribbon presence (5, 7).

Fusion of Synaptic Ribbon Precursors Is a Key Process in Presynaptic Maturation. Our data provide direct evidence that fusion of ribbons takes place at developing IHC AZs, hence clarifying the conundrum whether ribbon fusion or presynaptic pruning determine the morphological maturation that finally establishes AZs with predominantly single ribbons in IHCs (10). We propose that fusion of floating ribbon precursors to membrane-attached ribbons, as well as fusion of two neighboring membrane-anchored ribbons, provides cellular mechanisms to reduce ribbon numbers while regulating ribbon size and hence assures synaptic confinement. Interestingly, our 3D analyses of the basolateral compartment of several IHCs revealed comparable summed ribbon volumes per afferent contact between P9 and P34 IHCs, thereby suggesting that presynaptic RIBEYE levels—independent of actual ribbon number—remain remarkably constant during synapse maturation. However, mature ribbons exhibit an elongated shape (10, 17) and are capable of tethering an increased number of smaller-sized SVs to ensure efficient and indefatigable SV replenishment even during periods of ongoing activity. Alongside other structural and functional maturation steps—such as (*i*) the confinement of presynaptic Ca^{2+} channel clusters, (*ii*) the transition from Ca^{2+} micro- to nanodomain-like control of exocytosis, (*iii*) the maturation of SV reformation and glutamate loading pathways, and (*iv*) the postsynaptic merging and remodeling of PSDs and glutamate receptor patches (this study and ref. 10)—these processes likely result in the minimization of temporal jitter and thereby enable the exquisite temporal precision of synaptic transmission that is characteristic for mature IHC AZs.

In addition, our findings show that ribbon precursor formation occurs at a distance to the AZ as floating precursors with tethered SVs were found in the cytosol. Thus, while we cannot fully exclude a role of diffusional addition of individual cytosolic RIBEYE molecules (19, 46), we propose that the main mechanisms for developmental ribbon growth in mammalian IHCs is ribbon precursor fusion. It is tempting to speculate that the blockwise modulation of ribbon size—and concomitant SV tethering capacity—as observed here during development, may also present a form of presynaptic plasticity to accommodate for distinct states of activity. In this context, previous work on photoreceptor and pinealocyte ribbons suggested activity-dependent volume regulation of these presynaptic scaffolds that varied with illumination exposure (47–49). Such fusion and/or budding of SV-bearing ribbon blocks with membrane-anchored ribbons may present an efficient mechanism to rapidly modulate ribbon SV storage capacity in mature IHCs, likely exceeding the adaptive capacity provided by addition/loss of

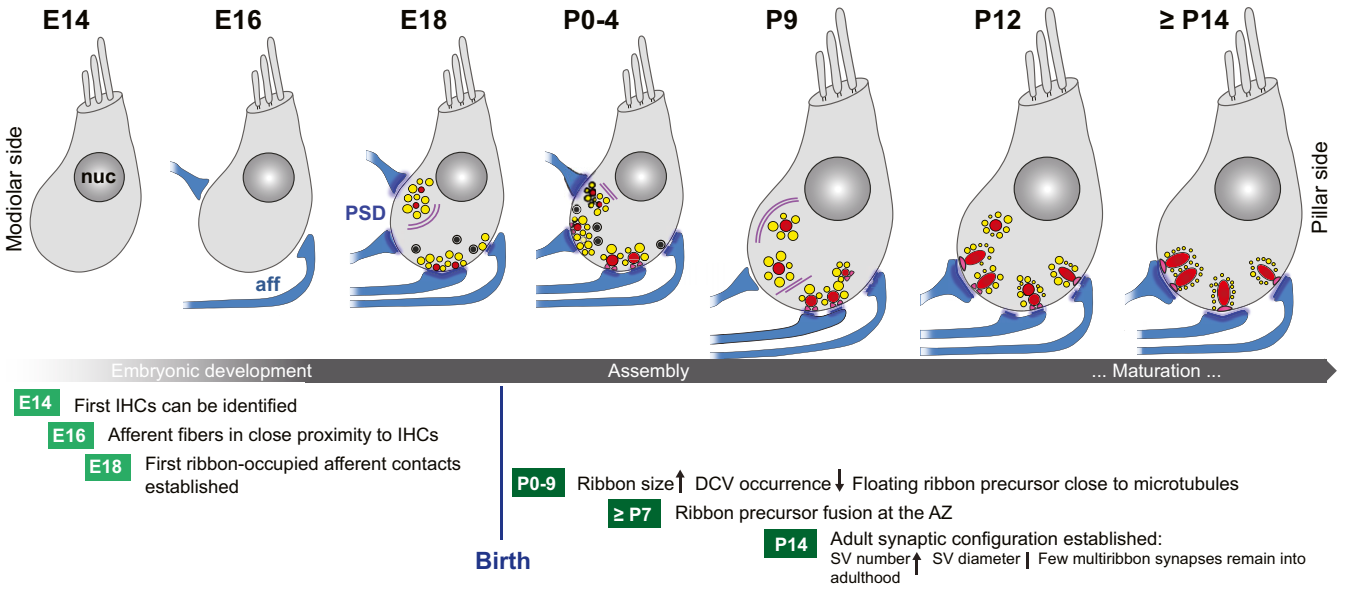

Fig. 8. Schematic summary of the key findings observed during developmental maturation of murine apical coil IHCs. Nuc, nucleus; aff, afferent fiber; PSD, postsynaptic density; light gray, IHCs; red, ribbon synapses; yellow, SVs; magenta, presynaptic density; purple lines, microtubules; black-filled circles, DCVs.

soluble RIBEYE. However, in the present study, the occurrence of cytosolic precursors was largely reduced once the final ribbon size was established at hearing onset. Moreover, the presence of fenestrated, hollow ribbons, which can be observed before P9 (this study and ref. 17) might indicate an aging process of synaptic ribbons suggestive of a limited lifetime of the structure as a whole. Therefore, future studies should investigate synaptic ribbon turnover rates in mammalian IHCs and assess the relative contributions of diffusional exchange of soluble RIBEYE molecules and blockwise addition/removal of ribbon material, respectively, for ribbon maintenance and plasticity after hearing onset.

The Molecular Identity of IHC Ribbon Precursors and Their Transport to the AZ. Early after birth, we found both SV-tethering ribbon precursors as well as DCVs close to IHC AZs, as reported previously (21). In contrast to piccolo-bassoon transport vesicles (PTVs) (32, 33), which mediate AZ assembly at conventional synapses, our immunogold analysis did not detect piccolino or CtBP2 labeling on DCVs of IHCs. In contrast, piccolino—alongside CtBP2—was found on floating ribbon precursors as well as membrane-attached ribbons in both immature and mature age groups, suggesting heteromeric molecular assembly within the cytosol before the translocation to the AZ. Hence, these data largely extend previous observations from retinal photoreceptors reporting piccolino expression at membrane-anchored ribbons (35, 36). We note that the observed DCVs were heterogeneous in size and their average diameter exceeds what has previously been published for PTVs (32). Therefore, we favor the hypothesis that AZs in IHCs are established via membrane attachment of ribbon precursors and is largely independent of PTVs. We propose that these DCVs may contain neurotrophins to guide neuronal pathfinding and boost SGN survival in the early postnatal organ of Corti. For example, Bdnf was detected in IHCs as well as outer hair cells (OHCs) until the age of ∼P10 and was additionally described in supporting cells at early postnatal ages (P1–P6) (50–52). Similarly, neurotrophin-3 (Ntf3) is found in postnatal and adult cochlear IHCs as well as supporting cells (50, 51, 53).

Independent of the analyzed age group, our observations indicate a predominantly basolateral synthesis of ribbon precursors in the cytosol. This finding contrasts with previous studies that reported the frequent occurrence of floating ribbon precursors in the supranuclear compartment of both IHCs—but mainly—OHCs (21). While this latter observation may suggest a role of the apically located Golgi apparatus in precursor synthesis, our data rather support the hypothesis of cytoplasmic RIBEYE self-assembly via RIBEYE–RIBEYE interactions (46–48, 54). However, such mechanisms are not mutually exclusive and moreover may be differentially regulated depending on maturational stage and tonotopic position of the IHC under investigation.

Finally, the mode of transport facilitating targeted delivery of native ribbons to the presynaptic AZ remained largely elusive. In this context, MTs have previously been described to terminate in close proximity to ribbon synapses of various cell types in different species (55–57) and our data now directly implicate MT-based transport in this process, likely involving the kinesin motor KIF1a. KIF1a has previously been shown to mediate SV precursor and DCV transport in neurons (58–60) and hence, may serve as a molecular linker between PA-SVs and MTs. Future studies will have to test this hypothesis in more detail.

Establishing Synaptic Heterogeneity: An Ultrastructural Perspective. It is commonly believed that the monosynaptic connections between IHCs and afferent SGNs are predominantly characterized by single ribbons decorating the presynaptic AZ. However, in an experimental tour de force, Merchan-Perez et al. previously showed that this general view might be too simplified, as ∼20% of ribbon synapses analyzed in adult cats still displayed multiribbon contacts (16, 41). Interestingly, these multiribbon contacts were innervated by low spontaneous rate SGNs contacting the modiolar (neural) side of these IHCs. Similarly, in the apical turn of the mouse organ of Corti, we observed a subpopulation of multiribbon contacts primarily at the modiolar side that was retained into adulthood and hence, our data corroborate the importance of this morphological feature and conservation across distinct species. This finding is significant since the occurrence of multiple ribbons per afferent contact strikingly increases the availability of SVs and likely also presynaptic Ca^{2+} channels. Moreover, given that synaptic ribbons appear to reach their final dimensions already around the onset of hearing, maximum ribbon size appears tightly regulated. Hence, multiple ribbons per AZ may offer a molecular bypass, allowing the strengthening of individual synapses.

Using FIB-SEM, we were able to reconstruct the entire basolateral compartments of several hair cells and analyze the developmental reorganization taking place prior and subsequent to hearing onset. This method allowed the analysis of several synaptic parameters in 3D and hence majorly extends previous work on this topic (16, 42–44, 61). Here, multiribbon afferent contacts could be detected—predominantly at the modiolar side of IHCs—across all age groups. In addition, our data indicate that over the transitional period around the onset of hearing, this spatial arrangement remains unchanged. Notably, in our P9 preparation, floating ribbon precursors could only be detected on the modiolar side, a finding that may, at least in part, result from the low sample size and number of animals inspected in this study and the tonotopic position of the IHCs under investigation. In addition, the observation of floating precursors on the pillar side may be statistically less probable due to the generally lower ribbon counts on this side. Consistent with our random sectioning data, ribbon size slightly increased for both the pillar and modiolar side, with a trend toward more and larger ribbons at the modiolar side. This is consistent with the findings of recent studies investigating presynaptic Ca^{2+} influx in murine IHCs (42, 44). Taken together, these data indicate that aspects of synaptic heterogeneity in IHCs are established early during maturation and before hearing onset. Moreover, location-dependent release capacity might directly contribute to the described functional differences observed in the firing properties of SGNs. The large modiolar AZs contain more Ca^{2+} channels, likely enabling high maximal rates of release, but operate at more depolarized potentials (44). Therefore, despite having more Ca^{2+} channels and SVs, modiolar AZs might actually release less at resting potentials and during weak stimulation, thereby offering a presynaptic hypothesis for the low spontaneous rate, high threshold SGNs. However, upon strong stimulation, their higher release capacity, in turn, might cause their vulnerability to excitotoxicity caused by noxious noise (62). In contrast, the smaller AZs at the pillar side show a more hyperpolarized operating range of presynaptic Ca^{2+} influx, which could explain the high spontaneous rate and low threshold of the postsynaptic SGNs (44). Future studies will be needed to test the presynaptic, postsynaptic, and efferent mechanisms that likely codetermine the firing properties of SGNs.

Materials and Methods

All experiments complied with national animal care guidelines and were approved by the University of Göttingen Board for Animal Welfare and the Animal Welfare Office of the State of Lower Saxony.

For detailed description of immunohistochemistry, confocal and superresolution STED imaging, conventional embedding and transmission electron microscopy, electron tomography, immunogold preembedding, SBF-SEM and FIB-SEM of the entire basolateral IHC compartment, and data analysis, see *SI Appendix*.

ACKNOWLEDGMENTS. We thank S. Gerke, C. Senger-Freitag, A. Goldak, A. Zeise, and C. Förster for expert technical assistance; O. L. Diaz for information technology support; M. Gültas for help with the statistical analysis of EM data; and M. Schifferer and the Electron Microscopy Hub at the German Center for

Neurodegenerative Diseases in Munich for FIB-SEM access and data acquisition support. This work was supported by German Research Foundation grants: Collaborative Research Center 889 [Projects A7 (to C.W.), A2 (to T.M.) and central funds (to C.V.)] and Niedersächsisches Vorab (T.M.). Part of this work (A.M.S.) was supported by the Cluster of Excellence and DFG Research Center Nanoscale Microscopy and Molecular Physiology of the Brain [Projects A1 (to W.M.) and A2 (to T.M.)]. This work was also supported by a Creutzfeldt Fellowship from the Elisabeth and Helmut Uhl Foundation (to C.V.) and additional funding from an intramural grant provided by the University Medical Center Göttingen (to C.V.).

1. Schmitz F, Königstorfer A, Südhof TC (2000) RIBEYE, a component of synaptic ribbons: A protein's journey through evolution provides insight into synaptic ribbon function. *Neuron* 28:857–872.
2. Khimich D, et al. (2005) Hair cell synaptic ribbons are essential for synchronous auditory signalling. *Nature* 434:889–894.
3. Frank T, et al. (2010) Bassoon and the synaptic ribbon organize Ca^{2+} channels and vesicles to add release sites and promote refilling. *Neuron* 68:724–738, and erratum (2010) 68:1202.
4. Sheets L, Trapani JG, Mo W, Obholzer N, Nicolson T (2011) Ribeye is required for presynaptic $Ca_{(V)}1.3a$ channel localization and afferent innervation of sensory hair cells. *Development* 138:1309–1319.
5. Jean P, et al. (2018) The synaptic ribbon is critical for sound encoding at high rates and with temporal precision. *eLife* 7:e29275.
6. Lenzi D, Crum J, Ellisman MH, Roberts WM (2002) Depolarization redistributes synaptic membrane and creates a gradient of vesicles on the synaptic body at a ribbon synapse. *Neuron* 36:649–659.
7. Becker L, et al. (2018) The presynaptic ribbon maintains vesicle populations at the hair cell afferent fiber synapse. *eLife* 7:e30241.
8. Buran BN, et al. (2010) Onset coding is degraded in auditory nerve fibers from mutant mice lacking synaptic ribbons. *J Neurosci* 30:7587–7597.
9. Mikaelian D, Ruben RJ (1965) Development of hearing in the normal Cba-J mouse: Correlation of physiological observations with behavioral responses and with cochlear anatomy. *Acta Otolaryngol* 59:451–461.
10. Wong AB, et al. (2014) Developmental refinement of hair cell synapses tightens the coupling of Ca^{2+} influx to exocytosis. *EMBO J* 33:247–264.
11. Roux I, et al. (2006) Otoferlin, defective in a human deafness form, is essential for exocytosis at the auditory ribbon synapse. *Cell* 127:277–289.
12. Johnson CP, Chapman ER (2010) Otoferlin is a calcium sensor that directly regulates SNARE-mediated membrane fusion. *J Cell Biol* 191:187–197.
13. Beurg M, et al. (2010) Control of exocytosis by synaptotagmins and otoferlin in auditory hair cells. *J Neurosci* 30:13281–13290.
14. Pangršič T, Reisinger E, Moser T (2012) Otoferlin: A multi-C2 domain protein essential for hearing. *Trends Neurosci* 35:671–680.
15. Huang L-C, et al. (2012) Synaptic profiles during neurite extension, refinement and retraction in the developing cochlea. *Neural Dev* 7:38.
16. Merchan-Perez A, Liberman MC (1996) Ultrastructural differences among afferent synapses on cochlear hair cells: Correlations with spontaneous discharge rate. *J Comp Neurol* 371:208–221.
17. Sobkowicz HM, Rose JE, Scott GE, Slapnick SM (1982) Ribbon synapses in the developing intact and cultured organ of Corti in the mouse. *J Neurosci* 2:942–957.
18. Regus-Leidig H, Tom Dieck S, Specht D, Meyer L, Brandstätter JH (2009) Early steps in the assembly of photoreceptor ribbon synapses in the mouse retina: The involvement of precursor spheres. *J Comp Neurol* 512:814–824.
19. Graydon CW, Manor U, Kindt KS (2017) In vivo ribbon mobility and turnover of Ribeye at zebrafish hair cell synapses. *Sci Rep* 7:7467.
20. Whitehead MC, Morest DK (1985) The growth of cochlear fibers and the formation of their synaptic endings in the avian inner ear: A study with the electron microscope. *Neuroscience* 14:277–300.
21. Sobkowicz HM, Rose JE, Scott GL, Levenick CV (1986) Distribution of synaptic ribbons in the developing organ of Corti. *J Neurocytol* 15:693–714.
22. Appler JM, Goodrich LV (2011) Connecting the ear to the brain: Molecular mechanisms of auditory circuit assembly. *Prog Neurobiol* 93:488–508.
23. Bulankina AV, Moser T (2012) Neural circuit development in the mammalian cochlea. *Physiology (Bethesda)* 27:100–112.
24. Koundakjian EJ, Appler JL, Goodrich LV (2007) Auditory neurons make stereotyped wiring decisions before maturation of their targets. *J Neurosci* 27:14078–14088.
25. Liberman MC (1980) Morphological differences among radial afferent fibers in the cat cochlea: An electron-microscopic study of serial sections. *Hear Res* 3:45–63.
26. Fariñas I, et al. (2001) Spatial shaping of cochlear innervation by temporally regulated neurotrophin expression. *J Neurosci* 21:6170–6180.
27. Kersigo J, Fritzsch B (2015) Inner ear hair cells deteriorate in mice engineered to have no or diminished innervation. *Front Aging Neurosci* 7:33.
28. Michael GJ, et al. (1997) Nerve growth factor treatment increases brain-derived neurotrophic factor selectively in TrkA-expressing dorsal root ganglion cells and in their central terminations within the spinal cord. *J Neurosci* 17:8476–8490.
29. Luo X-G, Rush RA, Zhou X-F (2001) Ultrastructural localization of brain-derived neurotrophic factor in rat primary sensory neurons. *Neurosci Res* 39:377–384.
30. Wu YJ, et al. (2004) Nerve growth factor, brain-derived neurotrophic factor, and neurotrophin-3 are sorted to dense-core vesicles and released via the regulated pathway in primary rat cortical neurons. *J Neurosci Res* 75:825–834.
31. Huttner WB, et al. (1995) Biogenesis of neurosecretory vesicles. *Cold Spring Harb Symp Quant Biol* 60:315–327.
32. Shapira M, et al. (2003) Unitary assembly of presynaptic active zones from Piccolo-Bassoon transport vesicles. *Neuron* 38:237–252.
33. Zhai RG, et al. (2001) Assembling the presynaptic active zone: A characterization of an active zone precursor vesicle. *Neuron* 29:131–143.
34. Pfenninger K, Sandri C, Akert K, Eugster CH (1969) Contribution to the problem of structural organization of the presynaptic area. *Brain Res* 12:10–18.
35. Limbach C, et al. (2011) Molecular in situ topology of Aczonin/Piccolo and associated proteins at the mammalian neurotransmitter release site. *Proc Natl Acad Sci USA* 108: E392–E401.
36. Regus-Leidig H, et al. (2013) Identification and immunocytochemical characterization of Piccolino, a novel Piccolo splice variant selectively expressed at sensory ribbon synapses of the eye and ear. *PLoS One* 8:e70373.
37. Hirokawa N, et al. (1989) Submolecular domains of bovine brain kinesin identified by electron microscopy and monoclonal antibody decoration. *Cell* 56:867–878.
38. Shen J, Scheffer DI, Kwan KY, Corey DP (2015) SHIELD: An integrative gene expression database for inner ear research. *Database (Oxford)* 2015:bav071.
39. Hirokawa N, Takemura R (2005) Molecular motors and mechanisms of directional transport in neurons. *Nat Rev Neurosci* 6:201–214.
40. Dick O, et al. (2001) Localization of the presynaptic cytomatrix protein Piccolo at ribbon and conventional synapses in the rat retina: Comparison with Bassoon. *J Comp Neurol* 439:224–234.
41. Kantardzhieva A, Liberman MC, Sewell WF (2013) Quantitative analysis of ribbons, vesicles, and cisterns at the cat inner hair cell synapse: Correlations with spontaneous rate. *J Comp Neurol* 521:3260–3271.
42. Frank T, Khimich D, Neef A, Moser T (2009) Mechanisms contributing to synaptic Ca^{2+} signals and their heterogeneity in hair cells. *Proc Natl Acad Sci USA* 106:4483–4488.
43. Liberman LD, Wang H, Liberman MC (2011) Opposing gradients of ribbon size and AMPA receptor expression underlie sensitivity differences among cochlear-nerve/hair-cell synapses. *J Neurosci* 31:801–808.
44. Ohn T-L, et al. (2016) Hair cells use active zones with different voltage dependence of Ca^{2+} influx to decompose sounds into complementary neural codes. *Proc Natl Acad Sci USA* 113:E4716–E4725.
45. Yin Y, Liberman LD, Maison SF, Liberman MC (2014) Olivocochlear innervation maintains the normal modiolar-pillar and habenular-cuticular gradients in cochlear synaptic morphology. *J Assoc Res Otolaryngol* 15:571–583.
46. Magupalli VG, et al. (2008) Multiple RIBEYE-RIBEYE interactions create a dynamic scaffold for the formation of synaptic ribbons. *J Neurosci* 28:7954–7967.
47. Fuchs M, Sendelbeck A, Atorf J, Kremers J, Brandstätter JH (2013) Strain differences in illumination-dependent structural changes at mouse photoreceptor ribbon synapses. *J Comp Neurol* 521:69–78.
48. Spiwoks-Becker I, Glas M, Lasarzik I, Vollrath L (2004) Mouse photoreceptor synaptic ribbons lose and regain material in response to illumination changes. *Eur J Neurosci* 19:1559–1571.
49. Vollrath L, Seidel A (1989) *The Plasticity of Synaptic Ribbons* (Biomed Res, Tokyo), Vol 10, pp 207–212.
50. Fritzsch B, Pirvola U, Ylikoski J (1999) Making and breaking the innervation of the ear: Neurotrophic support during ear development and its clinical implications. *Cell Tissue Res* 295:369–382.
51. Pirvola U, et al. (1992) Brain-derived neurotrophic factor and neurotrophin 3 mRNAs in the peripheral target fields of developing inner ear ganglia. *Proc Natl Acad Sci USA* 89:9915–9919.
52. Wiechers B, et al. (1999) A changing pattern of brain-derived neurotrophic factor expression correlates with the rearrangement of fibers during cochlear development of rats and mice. *J Neurosci* 19:3033–3042.
53. Sugawara M, Murtie JC, Stankovic KM, Liberman MC, Corfas G (2007) Dynamic patterns of neurotrophin 3 expression in the postnatal mouse inner ear. *J Comp Neurol* 501:30–37.
54. Schmitz F (2009) The making of synaptic ribbons: How they are built and what they do. *Neuroscientist* 15:611–624.
55. Mørup Jørgensen J (1982) Microtubules and laminated structures in inner ear hair cells. *Acta Otolaryngol* 94:241–248.
56. Gray EG (1976) Microtubules in synapses of the retina. *J Neurocytol* 5:361–370.
57. Graydon CW, Cho S, Li G-L, Kachar B, von Gersdorff H (2011) Sharp Ca^{2+} nanodomains beneath the ribbon promote highly synchronous multivesicular release at hair cell synapses. *J Neurosci* 31:16637–16650.
58. Okada Y, Yamazaki H, Sekine-Aizawa Y, Hirokawa N (1995) The neuron-specific kinesin superfamily protein KIF1A is a unique monomeric motor for anterograde axonal transport of synaptic vesicle precursors. *Cell* 81:769–780.
59. Lo KY, Kuzmin A, Unger SM, Petersen JD, Silverman MA (2011) KIF1A is the primary anterograde motor protein required for the axonal transport of dense-core vesicles in cultured hippocampal neurons. *Neurosci Lett* 491:168–173.
60. Yonekawa Y, et al. (1998) Defect in synaptic vesicle precursor transport and neuronal cell death in KIF1A motor protein-deficient mice. *J Cell Biol* 141:431–441.
61. Taberner AM, Liberman MC (2005) Response properties of single auditory nerve fibers in the mouse. *J Neurophysiol* 93:557–569.
62. Furman AC, Kujawa SG, Liberman MC (2013) Noise-induced cochlear neuropathy is selective for fibers with low spontaneous rates. *J Neurophysiol* 110:577–586.